DOI: 10.1021/ma101889s

Macromolecules
ARTICLE

Nanofibrillar Patterns by Plasma Etching: The Influence of Polymer Crystallinity and Orientation in Surface Morphology

Ellen Wohlfart,[†,∥] Juan P. Fernández-Blázquez,[‡,∥] Elisabeth Knoche,[†] Antonio Bello,[§] Ernesto Pérez,[§] Eduard Arzt,[⊥] and Aránzazu del Campo*[,‡]

[†]*Max-Planck-Institut für Metallforschung, Stuttgart, Germany,* [‡]*Max-Planck-Institut für Polymerforschung, Ackermannweg 10, 55128 Mainz, Germany,* [§]*Instituto de Ciencia y Tecnología de Polímeros (C.S.I.C.), Madrid, Spain, and* [⊥]*Leibniz Institut für Neue Materialien, Saarbrücken, Germany.* [∥] *These authors have contributed equally to this work*

Received August 17, 2010; Revised Manuscript Received October 21, 2010

ABSTRACT: This manuscript explores the possibility of exploiting polymer morphology (thermal or flow-induced) as materials inherent template, and domain-selective plasma etching as pattern developer, to obtain nanopatterned surfaces with different and controlled geometries, with a particular focus on nanofibrillar patterns. Oxidative plasma treatment of PET films has rendered patterned surfaces with different geometries depending on the crystallinity and orientation of the PET sample and plasma treatment time (or etching ratio). Homogeneous patterns with either randomly distributed or aligned nanofibrils with diameters between 20 and 40 nm and lengths up to 1 μm (after extensive etching) were observed depending on the sample pretreatment. Our results demonstrate the potential of oxidative plasmas as templateless nanopatterning technique and reveal a complex interplay between plasma etching parameters and polymer microstructure driving the pattern formation mechanism. These results open the possibility of fabricating gecko-inspired surfaces in a cost-effective manner.

Introduction

Nano- and microstructured surfaces found in nature (shark skin, lotus leaves, moth eyes or gecko feet) show interesting properties depending on their design and dimensions, such as reduced flow resistance, self-cleaning, antireflection or reversible adhesion. In order to transfer these natural principles to technical applications, different patterning techniques have been developed to generate micro and nanostructures on surfaces of polymer materials.[1] Most of these techniques come from the microelectronic industry and are lithography-based or require a costly template (mask or mold) to be performed, they require special equipment and infrastructure (i.e., clean room conditions, high vacuum), are time-consuming, expensive, and only applicable to structure small areas. There is no doubt that the implementation of such properties into consumer articles will require the development of more flexible, simple, time-saving and less costly patterning strategies for polymer materials. In particular, the generation of long, free-standing and hierarchically ordered nanofibrils, as required for the fabrication of gecko-inspired adhesive surfaces, will never be possible with any of the existing approaches.[2]

It is well-known that oxidative plasma treatment of polymer surfaces increases surface roughness.[3] The polymer surface in the plasma is exposed to a broad spectrum of ions, electrons, excited neutrals, radicals, UV, and VUV radiation that cause etching and, consequently, increase surface roughness and change surface chemistry. However, plasma roughening has not been regarded as a method for producing useful patterns. Recent published work has changed this view, and in fact, interesting regular surface topographies after plasma treatment of polymer surfaces under defined conditions have been recently reported. In semicrystalline polymers, nanometer-sized roughness were observed on cellulose fibers after oxygen plasma treatment,[4] microsized aligned walls,[5] nanosized bumps,[6] and fibrils[7] with 20 nm in diameter and up to 300 nm in length were observed after oxidative plasma treatment of PET films. Nanotextures have also been observed in amorphous polymers, i.e. in nanobumps and nanofibrils were obtained on polystyrene (PS) films using CF_4/O_2 plasma,[8] pins with 70−90 nm thickness and up to 600 nm height were obtained after Ar/O_2 plasma treatment of PMMA films,[9] and short and branched walls were reported in PP.[10] In PDMS quasi-periodic dimples with heights between 1.5 and 4.5 μm and a periodicity around 1.5 μm were shown after CF_4 plasma treatment,[11] ordered but randomly oriented high surface area nanostructures with controllable periodicity in the 50−200 nm range after O_2 plasma treatment,[12] and nanohairs after SF_6 plasma treatment.[13] Fibrils with dimensions ranging from 50 to 500 nm and lengths up to 5 μm were also reported after plasma treatment of spin-coated films of different materials[14] (PMMA, PS, PVDF, PEDOT, PPY, and SU-8 photoresist). These structured surfaces have been studied in terms of their resulting superhydrophobicity,[6,8b,10,11,15] antireflecting,[9] and cell-adhesive[16] properties. However, no significant attempts up to now have been made to control pattern formation in order to create defined patterns and make this method useful and transferable to other polymers.

Understanding pattern formation requires systematic studies of material and plasma processing variables influencing etching rates and mechanisms. No information can be extracted from existing literature, since the materials and plasma processing parameters used vary between different experimentators and a comparison of results is not possible. In this context, this manuscript studies the influence of polymer morphology (thermal and mechanically induced) in pattern formation. It demonstrates that it is possible to obtain different textures from the same polymer

*Corresponding author. Telephone: +49 (0)6131 379563. Fax: +49 (0)6131 379271. E-mail: delcampo@mpip-mainz.mpg.de.

 Published on Web 11/04/2010

material only by adjusting the polymer microstructure. Our studies focus on the generation of nanofibrillar patterns on semicrystalline, amorphous and oriented poly(ethylene terephthalate) (PET) samples and characterize the performance of the obtained nanofibrillar surfaces as gecko-like adhesives.

Experimental Section

Materials and Equipment. The following PET films were used: Thermanox (Nunc), Hostaphan (Mitsubishi), Mylar A (Du Pont), PET (ES301480 Goodfellow). PET granulate (CAT 04301) was purchased from Polysciences. Microstructured PDMS stamps were obtained as published.[17]

Compression molding was performed using a Collin press or a manual lab press PW 10 H (P/O/Weber, Remshalden, Germany). Thermal analysis of the films was performed by Differential Scanning Calorimetry using a DSC 822 (Mettler Toledo). Uniaxial tensile tests were performed with a home-built tensile device.[18] Wide-angle X-ray diffraction (WAXS) of the oriented fibers was performed with a Siemens flat-plate camera attached to a Phillips 2 kW tube X-ray generator using nickel-filtered Cu Kα radiation. Hot embossing was performed using a Präzitherm PZ 20 ET precision hot stage (Gestigkeit, Düsseldorf, Germany).

Plasma experiments were performed with a Plasma Activate Statuo 10 USB (plasma technology GmbH, Rottenburg, Germany). The characterization of the surface topography was performed using a Hitachi S-4800 or a LEO 1530 VP (Zeiss) scanning electron microscope. Samples were sputter-coated with gold−palladium using a BAL-TEC, SCD 500 Sputter Coater or carbon coated with MED 010, Balzers Union. Cross sections for SEM analysis were cut with a Leica EM UC6 ultramicrotome (Wetzlar, Germany) using an oscillating knife ultrasonic 35° from Diatome AG (Biel, Switzerland).

PET Films. PET films with controlled thermal histories were prepared by compression molding. The granulate was melted between Teflon sheets and the melt film was left at 1.5 MPa and 270 °C for 3 min. Amorphous films were prepared by rapid cooling the molten film between water-cooled plates. Semicrystalline films were obtained by slowly cooling the melt at 10 °C/min between the plates of the press at pressure between 0.5 and 1.5 MPa. Film thickness was in the range 100−250 μm.

Microstructured PET Films by Hot-Embossing. PET granulate was melted on a hot plate at 270 °C and a tempered PDMS stamp containing a regular pattern of microholes[17] was carefully pressed against it. The stamp was left between 3 and 30 min on the PET in order to allow mold filling without further pressure. Then the sample was cooled to room temperature, and the PDMS stamp was carefully peeled off from the PET film.

Uniaxial Stretching of PET Samples. Samples for uniaxial tensile tests were cut rectangular (width 3.43 or 6.43 mm, length 50 mm) or waisted (width 4.0 mm, length 50 mm) using a cutting die. Samples were stretched either directly or after annealing. For stretching, the samples were fixed with clamps at the tensile tester. The distance between the clamps was adjusted to 10 mm. Tensile tests were performed at 100 °C with stretching rates between 2 and 30 mm/min. Samples which broke at the beginning of the test were discarded. After stretching, samples were removed from the device within 1 min except those that received a poststretching annealing at 100 °C.

Plasma Treatment. A low pressure capacitively coupled plasma reactor operating at 24 kHz was used. Typical experimental conditions were oxygen pressure of 0.1 mbar and power 100 W. The chamber was connected to a computer that allows selection of the plasma conditions (pressure, power, and time) before the experiment. Sample size was typically 20 × 20 mm. During the experiment, the real-time profiles of the pressure in the plasma chamber and temperature at the electrode were monitored.

Plasma etching was also performed for polymer films that were tilted at 30°, 45°, and 60° with respect to the electrode by placing the sample on a metallic block on the plasma electrode.

Weight Loss. Squares with an area of 4 cm^2 were cut from PET films. The sample was weighted before, immediately after, and at selected times after the plasma treatment with a microbalance. Samples were stored in a closed Petri dish in the lab.

SEM. Plasma-treated films were placed on SEM pin stubs (Agar Scientific, Essex, U.K.) and sputter-coated with a 5 nm thick layer of AuPd or a carbon layer prior to SEM imaging.

Gold-Masked PET Micropatterns. Thermanox films were covered by TEM copper grids and sputter coated with 20 nm AuPd. The gold patterned sample was plasma treated and subsequently sputter coated with 5 nm AuPd. Small pieces with triangular shape were cut and embedded into Epofix resin for ultramicrotomy and carbon coated for SEM imaging.

Ultramicrotomy. A triangular shaped piece of the PET sample was embedded into an epoxy matrix and then trimmed to generate a pyramidal block. The block was clamped in the ultramicrotome and thin slices were cut with an oscillating knife with 0.6 mm/s. Slices with a thickness of 70−100 nm were obtained. They were connected at one point forming a band that slipped into a water basin which was attached behind the diamond knife. Then the slices were caught from the water bath using a TEM copper grid.

Characterization of Polymer by DSC. Measurements were performed at a scanning rate of 20 K/min. The melting enthalpy Δh^m was determined by integration of the melting endotherm around 250 °C. The degree of crystallinity of the PET samples was calculated using a value for melting enthalpy of 100% crystalline PET sample of $\Delta h_0^m = 125.6$ J/g.[19] The value of the glass transition temperature corresponds to the midpoint of the heat capacity increment observed in the DSC curves around 80 °C. The cold crystallization temperature corresponds to the peak value of the exothermal phenomena in the DSC melting curve.

Adhesion and Friction Measurements. Adhesion measurements were performed with a home-built indentation apparatus as described in ref 17. Macroscale friction measurements were performed using a slide equipment consisting of a board with adaptable angle to the horizontal moved by an electric motor. The films were cut into 1 cm^2 pieces and fixed to a cubic piece of wood (weight = 1 g) with a double sided adhesive tape. In order to avoid edge effects, the edges of the piece of wood were rounded, thus the foil also exhibited a light curvature. As counter surface we used either a glass slide or polymer plates with different surface roughness that were fixed to the movable board. These were positive replicas in epoxy resin (Spurr) obtained by casting negative replicas of sand paper made of dental wax (see ref 20 for details). During the measurement, the angle of the slide was increased at a speed of $\approx$2° per second until the sample started sliding. For each sample, the sliding angle was determined 10 times. Measurements were performed at a temperature of 24 °C and a humidity of 49%. For the measurement, plasma treated Thermanox samples under following conditions were used: 20 min oxygen plasma, 100 W, and 0.1 mbar.

Results

Commercially available biaxially oriented PET films were treated under similar plasma conditions as reported in the literature for which nanofibrils had been observed.[7] Nanoridges and nanofibrils were obtained on the PET surface (Figure 1). Both structures became visible at the same time. After 1 min plasma treatment, ridges of 5−10 nm width decorated with small bumps of 30 nm diameter appeared. Ridges were oriented in all directions. As etching proceeded, the height of the ridges between bumps decreased and the aspect ratio of the bumps increased. After 4 min, the surface structure consisted of fibrils interconnected by short ridges at their basement. Longer plasma times led to longer fibrils that became mechanically unstable and

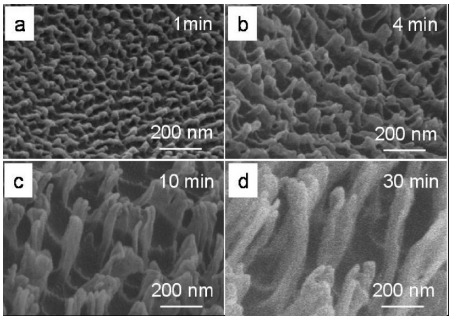

Figure 1. SEM images of PET (Thermanox) treated with oxygen plasma for (a) 1 min, (b) 4 min, (c) 10 min, and (d) 30 min. Plasma parameters were 30 W and 0.1 mbar. Samples were tilted 45° for imaging.

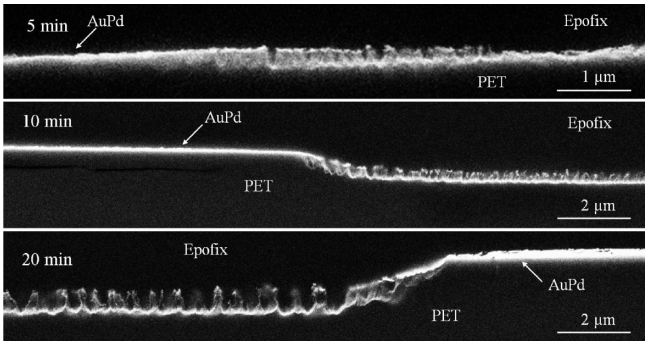

Figure 2. Cross sections of micro patterned and subsequently plasma treated PET samples (Thermanox). AuPd-coated regions appear flat.

condensed to form bundles. The onset for fibril condensation was observed after 4−6 min of plasma treatment, when the aspect ratio of the fibrils approached 3. After 30 min, fibril length increased to more than 900 nm. Similar surface structures and dimensions (data not shown) were also found in crystalline biaxially stretched PET films from other providers (Hostaphan-RN and Mylar A, see Figure A in the Supporting Information).

In order to visualize the etching profile, a gold−palladium pattern was sputtered onto the surface prior to plasma treatment (see Experimental Section for details). Figure 2 shows SEM images of cross sections obtained by ultramicrotomy containing AuPd coated and noncoated PET regions. Fibrils were clearly observed at the etched PET regions. After 5 min etching the top of the fibrils was at the same height as the gold layer, indicating that the material between the fibrils was preferentially removed during treatment. Increasing the plasma treatment time led to a linear increase of the etching depth (73 nm/min) and of the fibril length (30 nm/min) (Figure 3). The slower increase of the fibril length indicates that fibrils were also etched as plasma treatment time increased.

Study of Crystallinity Effects. Amorphous and semicrystalline (35% crystallinity degree as determined by DSC) PET films were self-prepared, plasma treated under equivalent conditions and weighted before and immediately after the treatment. A significant weight loss was detected in both samples after treatment (Figure 4). Below 10 min both samples showed a linear decrease of weight loss with plasma treatment time. The amorphous samples showed higher weight loss rate, indicating that the polymer chains in the amorphous state were etched more easily than in the crystalline state. At etching times longer than 10 min, the rate of weight loss of the amorphous sample was significantly slowed down. Deceleration was less significant in the semicrystalline sample. In fact, after 60 min of plasma treatment,

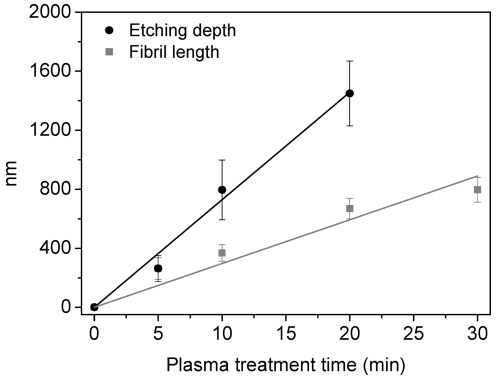

Figure 3. Variation of fibril length and etching depth with plasma treatment time on Thermanox PET film.

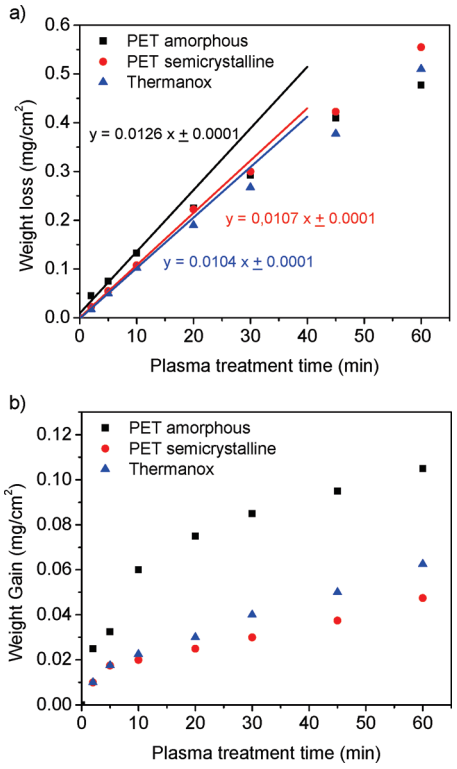

Figure 4. (A) Weight loss measured on amorphous and semicrystalline PET films and biaxially oriented semicrystalline PET (Thermanox) immediately after plasma treatment at 100 W and 0.1 mbar during different times. (B) Weight gain of same plasma-treated samples after 24 h exposure to ambient conditions.

the weight loss of the amorphous sample was lower than the weight loss of the semicrystalline sample.

Upon storage of the samples in a closed recipient at ambient conditions during 24 h a significant increase in the sample weight was detected. This indicates that the polymer surface remained reactive after plasma treatment and stabilized by absorbing or reacting with molecules from the atmosphere. Longer storage times did not lead to further changes. Weight gain in the amorphous sample after stabilization doubled that of the semicrystalline sample. Weight gain increased with plasma treatment time and this increase was more pronounced in the amorphous sample and during the first 10 min of plasma treatment. This tendency is parallel to the decelerated weight loss after 10 min treatment observed previously. It suggests that plasma treatment during the first 10 min induced a surface change in the amorphous

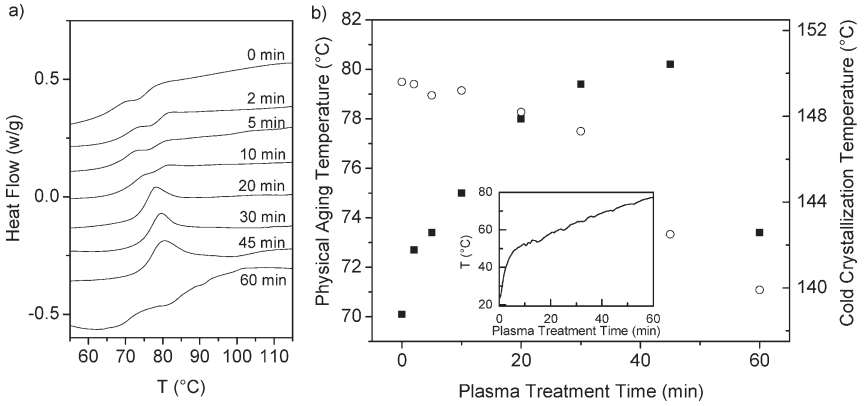

Figure 5. (A) DSC melting profiles of amorphous PET samples after different plasma treatment times at 100 W and 0.1 mbar. (B) Position of aging peak (full symbols) and cold crystallization temperature (open symbols) of amorphous PET samples after plasma treatment for different times. Inset: Temperature evolution of the electrode during plasma treatment at 100 W, 0.1 mbar for 60 min.

PET sample that led to higher etching resistance and lower plasma-induced surface chemical reactivity.

The inset in Figure 5 shows the temperature change at the electrode during the plasma experiment as a consequence of the bombardment flux of high-energy positive ions. A gradual increase up to 75 °C occurred after 60 min plasma treatment. The T increase is steeper during the first 10 min of plasma treatment. This could explain the steeper slopes observed in the weight loss and weight gain plots in Figure 4 below 10 min. We hypothesized that the T increase could also lead to ordering effects in the amorphous PET sample that could further slow down etching rate at longer plasma treatment times. In order to check this assumption, the thermal properties of the amorphous PET samples after plasma treatment at different times were analyzed by DSC and compared. Figure 5 shows the DSC profiles of the glass transition corresponding to PET samples after plasma treatment at different times. A weak shoulder at a temperature below T_g that moved to higher temperatures with increasing plasma treatment time was visible and appeared as a pronounced endothermic peak at 78 °C after 20 min plasma treatment (Figure 5). Such profile is characteristic of physical aging effects of supercooled polymer samples when stored at temperatures below T_g.[21] Note that the temperature at the sample during the plasma experiment approached 60 °C after 20 min treatment, as indicated in the inset in Figure 5a. After 60 min plasma treatment the endotherm appeared again as a weak shoulder below T_g, in agreement with the experimental observation that the temperature at the sample overcame T_g and physical aging effects during treatment were erased (only physical aging during storage is visible).

The position of the cold crystallization exotherm also showed a small variation with increasing plasma treatment times (Figure 5b). A shift to lower temperatures was visible and became more pronounced in the samples that had been plasma treated for longer than 10 min. This result indicates that the increase in temperature during plasma treatment allowed a certain degree of chain mobility and reorganization that facilitated posterior crystallization. No significant difference in the cold crystallization enthalpy was found between samples that were plasma treated during times below 45 min ($\Delta H = 46$ J/g). However, after 60 min plasma treatment the cold crystallization enthalpy was reduced to 40.4 J/g, indicating that the higher temperatures reached during the plasma treatment already allowed initiation of the crystallization process (up to 5%). The melting endotherm did not change with plasma treatment and had an enthalpy of 46.4 J/g corresponding to a degree of crystallinity of 37%.

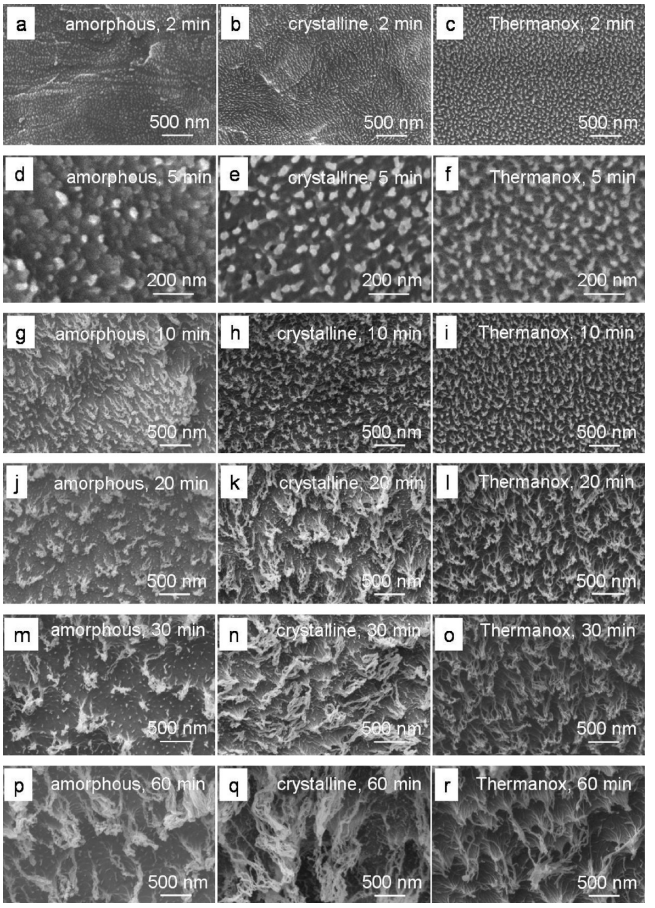

Figure 6. SEM images of amorphous, semicrystalline, and semicrystalline biaxially oriented PET films (Thermanox) after plasma treatment. All samples are tilted 30°. Note that magnification is different in pictures d−f.

The exposed results indicate that the increase of temperature during plasma treatment significantly changed the morphology of the amorphous PET sample. These changes may be responsible for the different evolution of the etching rate and weight gain observed in amorphous vs semicrystalline samples. These issues will be discussed later.

The surface topography of the amorphous and crystalline PET films after plasma treatment was analyzed by SEM and is compared in Figure 6. A transition from incipient fibrils to fibrils and fibrillar bundles was found in both samples.

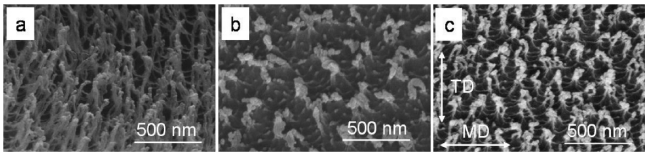

Figure 7. SEM images of commercial biaxially oriented PET films from different suppliers after 10 min oxygen plasma at 100 W and 0.1 mbar. Key: (a) Thermanox, crystallinity 35%, (b) Goodfellow, amorphous, and (c) Hostaphan RN, crystallinity 35%. Drawing directions of Hostaphan RN are indicated as machine direction (MD) and transverse direction (TD). Samples were tilted 30° for imaging.

Table 1. Thermal and Mechanical History and Crystallinity of Uniaxially Stretched PET Samples

mechanical treatment	thermal treatment after stretching, achieved crystallinity w_c
uniaxially stretched from amorphous	none, 19.7%
uniaxially stretched from amorphous	annealed 75 min at 100 °C in the tensile tester, 44.7%
uniaxially stretched from crystalline	none, 44.4%

The structures were less defined in the amorphous sample and fibril density in the semicrystalline sample was significantly higher. This tendency was also found when comparing amorphous and semicrystalline biaxially oriented PET after plasma treatment under identical conditions (Figure 7). These results indicate that the polymer microstructure influences material response to plasma treatment and, consequently, the obtained surface design. The thermal history of the sample and the temperature treatment that the sample undergoes during plasma treatment must be taken into account in order to understand the plasma-induced nanostructuring mechanism.

Study of Orientation Effects. Figure 4 compares the weight loss of nonoriented semicrystalline PET and a biaxially stretched semicrystalline PET (Thermanox) after plasma treatment. Both samples showed similar weight loss independent of the orientation history. Etching rates of 0.0104 and 0.0107 mg/cm^{2}min were obtained for the oriented and nonoriented samples respectively. After 10 min, the etching rate decelerated slightly. For comparison, a rate of 0.003 mg/cm^2 min had been reported in the literature for oxidative plasma treatment of amorphous biaxially oriented PET samples using a glow discharge plasma (15 kHz, 0.067 mbar, 36 W, 1 sccm O_2).[22] Weight gain of oriented and nonoriented samples 24 h after treatment was also similar (Figure 4).

Figure 6 shows the surface structures of the biaxially oriented and nonoriented semicrystalline films. Similar fibrillar structures were observed in both samples, but fibrils were better defined and more homogeneously distributed in the biaxially oriented sample.

In order to further investigate a possible influence of sample orientation in the surface topography, a series of experiments with uniaxially oriented PET samples with controlled thermal histories and orientation were prepared. Amorphous and semicrystalline samples were stretched at a temperature above T_g (100 °C) and, if required, annealed at the same temperature maintaining the sample in the tester under load. The degree of orientation and the crystallinity were analyzed by X-ray diffraction (Figure B in the Supporting Information) and DSC (Table 1) experiments on the stretched fibres. Higher orientation degree was obtained in the oriented semicrystalline samples, with better defined

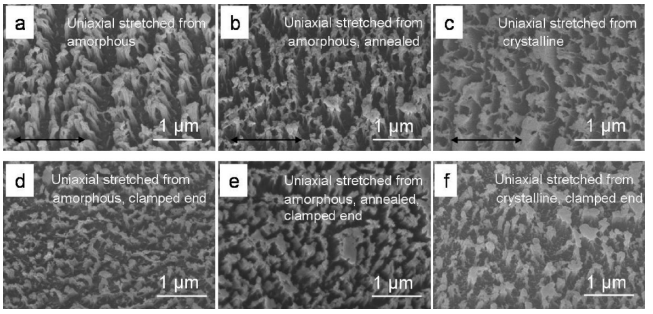

Figure 8. SEM pictures of PET surfaces after uniaxial stretching and subsequent plasma treatment (the black arrow indicates stretching direction). (a) Stretched from amorphous film, (b) stretched from amorphous film and annealed in the tensile tester after stretching, and (c) stretched from semicrystalline film. (d−f) Piece of the clamped end (no orientation) of the samples a−c after plasma treatment. Treatment conditions were 10 min at 100 W and 0.1 mbar. Samples were tilted 30° for imaging.

diffraction spots concentrated at the equator (see diffractograms in Figure B in the Supporting Information).[23] The stretching process at 100 °C induces crystallization of the amorphous sample. Annealed samples after stretching showed an enhancement of intensity of the diffraction spots and higher crystallinity.

Figure 8 shows the obtained surface structures after plasma treating the stretched samples. For comparison, both the surface structure of the oriented parts and the surface structure of nonoriented parts of the sample (from the clamped end during stretching) are shown. The black arrow indicates the stretching direction. All stretched samples showed nanofibrils, both at the clamped end and at the elongated parts. In the oriented sample from the amorphous film, the nanofibrils in the stretched region appeared aligned forming rows. Row direction was perpendicular to the stretching direction. This superstructure could not be found at the surface of the clamped end, suggesting that it is a consequence of the orientation process and not of the thermal treatment. If the oriented sample was annealed after stretching, the fibrils were no longer aligned. The semicrystalline sample stretched after crystallization also showed aligned fibrils. Neither semicrystalline nor amorphous biaxial oriented samples from different providers showed such alignment of the fibrils (Figure 7).

Adhesion and Friction Properties of Obtained Nanofibrillar Surfaces. Force−distance curves were measured on flat and nanofibrillar PET samples (Figure D in the Supporting Information). The monitored pull-off forces (P_c) are a measure of the adhesion of the surface. A P_c of 350 μN was obtained for the flat surface. The pull-off event in the nanofibrillar surface could not be detected, indicating that the surface adherence was significantly reduced by the plasma treatment. This is due to the low density of fibrils generated, which causes a dramatic decrease in the contact area that cannot be counteracted by the adhesion enhancement expected from the contact splitting.[24]

Figure 9 shows the friction coefficient of Thermanox samples measured against substrates with different roughness under two different humidity conditions. The friction coefficient decreases from 0.45 to 0.3 with increasing surface roughness up to 1 μm. Above 1 μm the friction coefficient remained constant. An increase in humidity from 47 to 61% resulted in lower friction coefficients. Plasma treated samples showed similar friction coefficients to flat films on substrates with roughness below 0.2 μm. However, the friction coefficient increased up to a value of 0.6 on substrates with higher

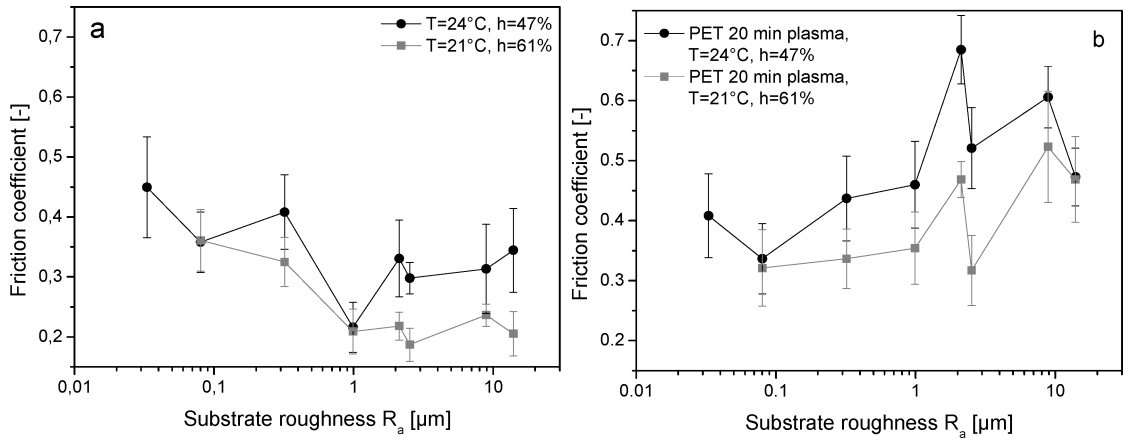

Figure 9. Friction coefficient measured on flat and nanostructured PET films (Thermanox) in contact with substrates with different roughness.

surface roughness. Note that the fibril diameter of the samples was around 140 nm (fibril bundles). As observed in the non structured surfaces, an increase in humidity led to lower friction.

Friction experiments were also performed on plasma treated samples where the fibrillar structures were tilted. The friction coefficients were measured by pulling the sample along and against the tilting direction of the fibrils. Plasma-treated samples always showed higher friction values than flat ones. However, no significant difference in the friction coefficients in the different directions could be detected.

Discussion

Reactive ion etching (RIE) of PET films has generated a surface topography containing bumps, ridges, isolated fibrils and condensed fibrils in the form of bundles. At low levels of etching bumps were observed, which further developed into fibrils with increasing aspect ratio as etching proceeded. The diameter of the bumps and fibrils typically varied between 15 and 40 nm and the distance between features from 20 to 50 nm. As fibrils reached an aspect ratio of about 3, they became mechanically unstable and started to collapse and stick together forming bundles. The number of fibrils in the bundles increased with etching time. Fibril bundles reached heights of up to 1 μm. Depending on the sample's thermal and mechanical history, these features were either located randomly across the surface, or they were aligned in a preferential direction (Figure 8a).

The transition from bumps to fibrils with increasing etching is smooth, as depicted in figure 6. This evolution suggests that initial bumps that appeared at low etching ratios are etched more slowly than the surrounding material and act as masks. As a consequence, the bump pattern is transferred vertically in the material by anisotropic etching and produces long fibrils at higher etching times. Two questions remain open: what is the nature of the bumps and why do they present lower etching rates than the surrounding matrix.

The anisotropy of the etching process was also confirmed by plasma treating PET films placed on a tilted disposition to the electrode. SEM analysis of the sample rim showed tilted nanofibrils (Figure C in the Supporting Information). Tilting angle of the fibrils varied depending on the inclination of the sample stage during plasma treatment. These results corroborate that etching is directional and, therefore, physical etching due to directed ion bombardment is influencing the structure formation mechanism under our experimental conditions.

According to our results, etching rate decelerates after 10 min plasma treatment (Figure 4A). This tendency is parallel to the decelerated temperature increase measured at the electrode during the experiment at plasma treatment times >10 min (inset in Figure 5B). It is important to note that RIE of a materials surface involves two main elementary processes or mechanisms: chemical etching, caused by the interaction of free radicals with the surface, and physical etching caused by accelerated cations. At film temperatures <100 °C the physical etching rate of polymer films has been reported to depend only to a small degree on substrate temperature.[25] However, chemical etching is temperature dependent in this range and, in fact, higher etching rates with increasing temperature (< 100 °C) have been reported during RIE of different polymer materials.[25,26] Our results reveal a significant contribution from chemical processes during our plasma experiment. The ratio of chemical to physical etching does not remain constant during the process but increases with plasma treatment time, as electrode temperature increases. It is important to note that chemical etching is not anisotropic and, therefore, may contribute negatively to the development of well-defined and high aspect ratio structures. Experiments with controlled electrode temperature are in progress.

The weight gain vs time dependence (Figure 4B) also shows a slope change in samples plasma treated for longer than 10 min, indicating that the increment in the reactive species at the surface for longer plasma treatments is also influenced by the rate of temperature increase at the electrode and the chemical/physical etching ratio.

Different Surface Structures Depending on Crystalline Morphology. Visible differences in the etching rate and resulting surface structures were found between amorphous and semicrystalline samples. Assuming that the differences in the etching rate between amorphous and semicrystalline PET are due to differences in the etching rate of amorphous and crystalline regions, and considering semicrystalline PET a two-phase material, we estimated the etching rate of the crystalline domains from the formula[27]

$$v_e = cv_{e,c} + (1-c)v_{e,a} = (v_{e,c} - v_{e,a})c + v_{e,a}{}^{27b} \quad (18)$$

where v_e is the total etching rate (77.8 nm/min as measured in the semicrystalline PET), $v_{e,c}$ is the etching rate of the crystalline phase, $v_{e,a}$ is the etching rate of the amorphous phase (94.5 nm/min as measured in the amorphous PET), and crystalline fraction c (35% in our semicrystalline PET samples). This model assumes that etching rate remains constant with time. Therefore, etching rates v_e and $v_{e,a}$ were obtained by fitting the data from figure 4 at treatment times below 10 min. Taking 1.455 g/cm^3 [28] and 1.333 g/cm^3 [29] as values for the density of 100% amorphous and 100% crystalline PET, an etching rate $v_{e,c}$ = 46.9 nm/min was calculated

for the crystalline fraction. The difference between $v_{e,a}$ and $v_{e,c}$ determines the selectivity of the etching process. It is important to note that this calculation does not consider temperature effects, changes in surface chemistry and roughness during treatment or surface restructuring. As such, the calculated etching rates should only be taken as indicative.

According to our results, the more pronounced deceleration of the etching rate obtained in amorphous PET at plasma treatment times >10 min can be a consequence of morphology changes in the sample induced by the increase in temperature (aging). Aging effects involve reorganization of the polymer chains in the amorphous state at temperatures close to T_g to form densified regions. These regions seem to be more resistant to plasma etching than amorphous domains. As aging and etching proceed during the plasma treatment, the surface is enriched in densified domains and the overall etching rate (as given by the weight loss) decreases. At the same time, fibrillar structures become more defined as a consequence of a masking effect at the densified regions.

It is important to note that the surface T_g of PET is expected to be lower than that of the bulk. In fact, a surface T_g of 56 °C has been reported for PET.[30] The oxidative plasma treatment may cause chain scission and a decrease in the molecular weight at the surface and, in turn, further lower surface T_g (a surface T_g of 53 °C has been reported for PET after 30 s oxygen plasma treatment at 13.54 MHz, 50 W, 6.7×10^{-4} mbar[30]). This means that aging effects at the surface may start at lower temperatures than in the bulk and occur faster.

Physical aging takes place when a polymer is in a nonequilibrium state (i.e., supercooled) and is caused by molecular relaxations that are biased in the direction required to drive the material closer to equilibrium. Aging occurs in the amorphous state but does not easily occur in the amorphous domains of crystalline samples where chain mobility is highly constrained due to the presence of crystallites. Accordingly, semicrystalline PET does not show the same effects (Figure 4A).

Our hypothesis assumes that the morphology of the PET film is homogeneous across the film thickness. However, there is recent evidence in the literature claiming differences in the degree of crystallinity at the surface and in the bulk.[31] The formation of a "skin layer" a few micrometers thick with different properties from the bulk is plausible if processing conditions involve rapid cooling, as in the amorphous quenched PET film. Cooling at the surface will be faster and, therefore, incipient ordering processes may increase in the interior of the film. This could also explain a decrease in the etching rate with increasing etching depth in the amorphous film.

It is important to point out that semicrystalline PET cannot be described by a simple two-phase model of crystalline and amorphous domains.[32] The morphology of semicrystalline PET is complex and has been demonstrated to contain varying amounts of intermediate ordered morphologies. There, the PET chains are only partially ordered and constrained due to the crystalline domains. The ratio and type of mesomorphic domains strongly depend on the thermal and orientation history (draw temperature and draw rate) of the sample. We hypothesize that these mesophases will present intermediate etching rates between the purely amorphous and purely crystalline domains and blur surface patterns.

Changes in the Surface Structures by Mechanical Pretreatment. Nonoriented, uniaxially, and biaxially oriented PET films showed distinct differences in the surface topography after oxidative plasma treatment. The dimensions of the fibrils were similar in all cases, but fibrils were better defined and more homogeneously distributed in the oriented samples (see Figures 6−8). Assuming that the fibrils may result from differential etching of domains with differing morphology, it seems that ordered domains are better defined in the oriented samples and this enhances the response to and selectivity of the etching process.

The fibrils in uniaxially stretched samples were aligned in rows perpendicular to the stretching direction (Figure 8a), demonstrating the possibility of exploiting the mechanical pretreatment to obtain a hierarchical arrangement of surface nanofeatures in a single plasma process. Annealed samples after mechanical treatment did not show aligned fibrils, indicating that the final topography results from mechanical and thermal factors. During annealing different phenomena take place, such as chain relaxation, reorganization of amorphous segments, chain transport, crystallization of amorphous domains, and improvement of crystalline regions. As a result, the microstructure of the PET sample relaxes and evolves into a more stable state closer to thermal equilibrium, forgetting to some extent the mechanical pretreatment. As a consequence, thermal annealing blurred the pre-existing orientation-related pattern for the plasma process.

It is important to note that the mechanical history of a sample strongly influences its crystalline morphology. Recently reported work on flow-induced morphology of uniaxially stretched amorphous PET above T_g claims that crystalline, amorphous and mesomorphic phases coexist in the stretched sample depending on stretching rate, ratio, and temperature.[33] When stretching amorphous PET at low stretch ratios, isotropic crystallites form and are embedded in an amorphous isotropic matrix. For larger stretching, anisotropic fibrillar domains orient along the stretching direction with crystallites forming a layered structure within the fibrillar domain. This structure is also present in oriented semicrystalline PET, although in this case orientation of the chains is preceded by the breaking of isotropic crystals. At higher stretching ratios, crystallites are oriented and more crystallites develop within the fibrillar domains. A significant proportion of the material still remains nonoriented.

Fibrils in biaxially oriented films were interconnected by ridges that seemed oriented in random directions. Ridges and walls seem to be etched faster than fibrils, but slower than the surrounding matrix. We hypothesize that these ridges could originate from etching of the anisotropic fibrillar domains (mesomorphic phase). More experiments on stretched samples under different and controlled stretching conditions would be required to prove this hypothesis.

Insights in Plasma-Induced Nanostructure Formation Mechanism. Different mechanisms of fibril formation in polymers upon plasma treatment have been proposed in the literature. For PET, the following mechanisms have been postulated: (i) differential etching of crystalline and amorphous domains,[34] (ii) dewetting of a polar fluid film of oxidized low molecular weight fragments in small drops that act as etch masks,[7] and (iii) redeposition of degraded material in atmospheric plasmas.[35] For other polymers further mechanisms have also been discussed: (iv) differential etching of crystalline and amorphous domains in cellulose fibres[15] and PP,[10] (v) sputtered Al particles from the plasma reactor wall that redeposit onto the surface of the polymer and act as masks during plasma etching of PMMA and PEEK,[36] (vi) anisotropic ion bombardment of the polymer surface owing to local variation in curvature[14a] (experiments were performed on spin-coated PMMA, PS, PVDF, PEDOT, PPY and photoresist materials), (vii) spontaneous perturbation and topography formation of a thin film of polymer melt as a

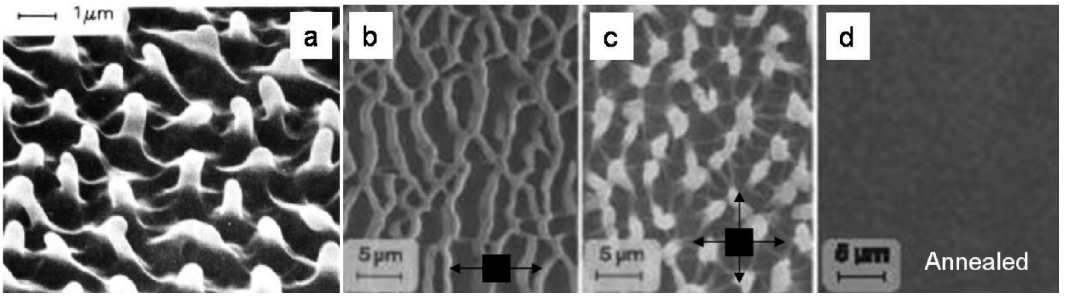

Figure 10. PET surface morphology after different kinds of treatment: (a) Treatment with ArF excimer laser generated fibrillar structures on biaxially oriented PET. (Reprinted with permission from ref 42b. Copyright 1986 American Chemical Society.) (b, c) Exposure to KrF laser radiation generates (b) wall-type structures in uniaxial and (c) nap-type structures in biaxial stretched samples which are perpendicular to the stretching directions. (Reprinted with permission from ref 44. Copyright 2000 Elsevier.) (d) In annealed films no structures were observed after exposure to KrF laser radiation. (Reprinted with permission from ref 45. Copyright 2000 Springer Science + Business Media).

consequence of surface instabilities induced by the electric field,[14b,37] or of buckling instabilities[38] (viii) no reference to any mechanism.[8b,11,39]

None of the reported works has been able to prove their hypothesis with convincing experimental data. Comparison between authors is difficult, since plasma chambers and operating conditions vary from author to author. In addition, the polymer samples used for their analysis are usually commercial and there is no exact information about their thermal and mechanical pretreatment or the presence of additives or fillers.

Under our experimental plasma conditions, our results demonstrate a clear influence of the polymer microstructure in the obtained surface topography and support the idea of differential etching between domains with different degree of order. However, etching differences between the domains are small and seem to be only detectable within a certain range of plasma parameter. Analysis of the internal structure and composition of the fibrils with TEM could provide information to consider or refute the dewetting, redeposition, Al-sputtering or surface-instabilities hypothesis. In the first three cases a different chemical composition of the tip and the rest of the fibril should have been observed. In the last case, chain flow under the electric field should yield fibrils formed by highly oriented chains. This will be part of our future work.

Comparison of Surface Topographies Observed on PET after Etching with Other Methods. There are a few reports in the literature concerning surface treatment of PET with different etching methods that have also generated distinct surface topographies. Chemical etching of mono- and biaxially stretched PET films (from amorphous at 100 °C) using *n*-propylamine as solvent has generated a surface microstructure with interconnected ridges.[40] The width of the ridges was about 15 nm and the mean length between interconnections was about 150 nm. Bigger structures up to 1 μm in length were also found depending on sample history. These dimensions are similar to ours at low etching ratios. In uniaxially stretched samples, ridges were oriented perpendicular to the stretching direction.[40] The orientation improved with the stretching ratio. Biaxial orientation generated randomly oriented ridges. Ridges have also been observed when wearing the surface of uniaxially and biaxially oriented PET films with an AFM tip in contact mode above a certain load.[41] Inter-ridge spacing was 100 nm and increased up to 200 with increasing AFM tip load. No correlation with the drawing direction was seen in this case, probably because of the small size of the scanned field (1 μm^2).

Several authors have reported ridged, bump, and short fibrillar structures upon increasing photoablation of semi-crystalline PET films using an excimer laser.[42] Feature's geometry resembles our obtained structures, but lateral dimensions are bigger (fibril diameter about 1 μm) (Figure 10a).[42] The authors attribute the formation of the short fibrils to the crystalline subsurface morphology, since they did not observe them in amorphous PET samples. Other authors attribute ridge formation under similar conditions to the development of cracks during radiation exposure due to stress accumulated within the material during stretching.[43] They observed ridges aligned in one direction on uniaxially drawn samples, aligned in two directions on biaxially drawn samples, and no ridges on annealed samples. Differences between crystalline and amorphous material were not considered and no explanation for the occurrence of fibrils was given. Their fibrils (Figure 10b−d)[44,45] strongly resemble the condensed fibrils resulting from some of our plasma conditions.

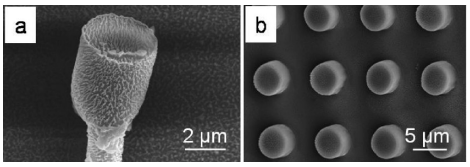

Figure 11. Hierarchical structures on PET generated by hot embossing and posterior plasma treatment.

In atmospheric plasma using argon as etching gas (etching rate 1 to 4 nm/min), biaxially oriented PET films showed oriented ridges aligned perpendicular to the second drawing direction with ca. 50 nm period and 30 nm width, decorated with globular features on the top that resembled incipient fibrils.[5] In uniaxially oriented film, similar features were obtained. Alignment was less clear, but appeared to be induced perpendicular to the draw direction.[5] It is important to note that etching in atmospheric plasmas is supposed to be only chemical and, therefore, isotropic.

The similarity between the surface structures obtained from the different etching methods supports our hypothesis that the structure formation mechanism relies on a pre-existing sample morphology that becomes visible upon etching under defined experimental conditions.

Increasing Complexity in Surface Patterns. Our results obtained with uniaxially oriented PET samples (Figure 8a) or on tilted films (Figure B in the Supporting Information) evidence the potential of this technique to obtain complex surface designs containing hierarchical arrangements of nanofeatures. This occurs in the absence of templates like molds or masks, and in a single patterning step. Figure 11 shows additional results where a micropatterned PET film obtained by hot-embossing was plasma treated to obtain

nanofibrils on the top of micropillars, proving the possibility of increasing pattern complexity by combining the plasma treatment with other micropatterning strategies.

Adhesive and Frictional Properties. Our nanofibrillar surfaces showed lower adhesion than the original, flat films. This can be attributed to the low density of fibrils on the surface obtained under our plasma conditions, which significantly reduced the effective contact area and, therefore, adhesion. This decrease could not counteracted by the adhesion enhancement expected from the high number of contact elements, as in the gecko.[24] Fibrillar patterns with higher coverage need to be generated in order to obtain better adhesive performance. In addition, gecko setae are placed on a compliant substrate, and this has been demonstrated to be a key element for the adhesive performance of artificial nanofibrillar surfaces.[46] This is not the case for our fibrils, which are attached to a hard PET backing layer. Experiments are in progress in order to obtain thin PET films on the top of a softer substrate in order to improve these issues.

Our nanofibrillar surfaces displayed higher friction than flat surfaces in the presence of roughness. The fibrillar topography allows better adaptation and contact to surfaces, provided that the surface features are bigger than the fibril diameter. This is also what we observed in our results. Friction coefficients of fibrillar surfaces onto substrates with roughness below 200 nm are similar to those measured on the flat PET surface. Note that friction coefficients between 0.25 and 5 have been found for other gecko-like surfaces made of polymeric nanofibrils or carbon nanotubes.[47] These surfaces presented higher density of nanofibrils than our substrates.

Conclusions

Polymer surfaces can be nanostructured by means of oxidative plasmas. This method is rapid, cheap, and can pattern large area samples (depending on the size of the electrode) with high aspect ratio fibrils at low cost. Patterns with randomly or hierarchically distributed nanofibrills were obtained on PET films. A complex interplay between etching rate and polymer morphology (thermal and flow-induced) is responsible for the pattern geometry. Our results demonstrate that plasma etching can be regarded as a flexible and effective templateless patterning technique. However, more studies need to be conducted in order to fully understand the pattern-generation mechanism and be able to control fibrillar design and geometry and enable wide application. For improving the performance of fibrillar, gecko-like adhesive surfaces, higher fibril coverage will be required. This might be obtained by a careful selection of materials and plasma parameters. Future work in our group will tackle these issues.

Acknowledgment. We thank Dr. S. Bloss (MPI für Metallforschung) for preliminary experiments, J. Eisenlohr and T. Ahlinger (Plasma Technolgy) for support and discussions, Dr. C. Greiner for providing the PDMS stamps for hot embossing, and Dr. P. Munzert (Fraunhofer Institut für Angewandte Optik und Feinmechanik, Jena, Germany) for discussion. J.P.F.-B. is indebted to Alexander von Humboldt Foundation for his research fellowship. The financial support of MICINN (Project MAT2007 65519-C02-01) is also gratefully acknowledged.

Supporting Information Available: A table giving the experimental details of uniaxial tensile test and figures showing the number of fibrils/fibril bundles per μm^2, WAXS diffractograms of PET samples, SEM images at the rim of the PET film, and load-displacement curves. This material is available free of charge via the Internet at http://pubs.acs.org.

References and Notes

(1) del Campo, A.; Arzt, E. *Chem. Rev.* **2008**, *108*, 911–945.
(2) Boesel, L. F.; Greiner, C.; Arzt, E.; del Campo, A. *Adv. Mat* **2010**, *22*, 2125–2137.
(3) d'Agostino, R.; Favia, P.; Oehr, C.; Wertheimer, M. R. *Plasma Processes and Polymers*: Wiley VCH: New York, 2005.
(4) Balu, B.; Breedveld, V.; Hess, D. *Langmuir* **2008**.
(5) Beake, B. D.; Ling, J. S. G.; Leggett, G. J. *J. Mater. Chem.* **1998**, *8*, 1735–1742.
(6) Teshima, K.; Sugimura, H.; Inoue, Y.; Takai, O.; Takano, A. *Langmuir* **2003**, *19*, 10624–10627.
(7) Powell, H. M.; Lannutti, J. J. *Langmuir* **2003**, *19*, 9071–9078.
(8) (a) Di Mundo, R.; Palumbo, F.; d'Agostino, R. *Langmuir* **2008**, *24*, 5044–5051. (b) Di Mundo, R.; Palumbo, F.; d'Agostino, R. *Langmuir* **2010**, *26*, 5196–5201.
(9) Leitel, R.; Kaless, A.; Schulz, U.; Kaiser, N. *Plasma Process. Polym.* **2007**, *4*, S878.
(10) Youngblood, J. P.; McCarthy, T. J. *Macromolecules* **1999**, *32*, 6800–6806.
(11) Manca, M.; Cortese, B.; Viola, I.; Aricò, A. S.; Cingolani, R.; Gigli, G. *Langmuir* **2008**, *24*, 1833–1843.
(12) Tsougeni, K.; Tserepi, A.; Boulousis, G.; Constantoudis, V.; Gogolides, E. *Plasma Process. Polym.* **2007**, *4*, 398–405.
(13) Tserepi, A.; Vlachopoulou, M. E.; Gogolides, E. *Nanotechnology* **2006**, *17*, 3977–3983.
(14) (a) Morber, J. R.; Wang, X.; Liu, J.; Snyder, R. L.; Wang, Z. L. *Adv. Mater.* **2009**, *21*, 2072–2076. (b) Northen, M. T.; Turner, K. L. *Nanotechnology* **2005**, *16*, 1159–1166.
(15) Balu, B.; Breedveld, V.; Hess, D. W. *Langmuir* **2008**, *24*, 4785–4790.
(16) Powell, H. M.; Kniss, D. A.; Lannutti, J. J. *Langmuir* **2006**, *22*, 5087–5094.
(17) Greiner, C.; del Campo, A.; Arzt, E. *Langmuir* **2007**, *23*, 3495–3502.
(18) Puente, P.; Delgado, R.; Moñivas, S. *Rev. Plast. Mod.* **2004**, *88*, 46.
(19) Wunderlich, B. *Macromolecular Physics. Crystal Structure, Morphology, Defects*; Academic Press: New York, 1973; Vol. *1*, p 389.
(20) Spurr, A. R. *J. Ultrastruct. Res.* **1969**, *26*, 31–43.
(21) White, J. R. *C. R. Chim.* **2006**, *9*, 1396–1408.
(22) Weikart, C. M.; Yasuda, H. K. *J. Polym. Sci., Polym. Chem.* **2000**, *38*, 3028–3042.
(23) Viana, J. C.; Mano, J. F.; Denchev, Z. Z.; Oliveira, M. J.; Cramez, M. C. *Adv. Mater. Forum III, Parts 1 and 2* **2006**, *514−516*.
(24) Arzt, E.; Gorb, S.; Spolenak, R. *Proc. Natl. Acad. Sci. U.S.A.* **2003**, *100*, 10603–10606.
(25) (a) Dems, B. C.; Rodriguez, F. *J. Vac. Sci. Technol. B* **1990**, *8*, 1985–1989. (b) Pons, M.; Joubert, O.; Paniez, P.; Pelletier, J. *J. Appl. Phys.* **1991**, *70*, 2376–2379.
(26) (a) Egitto, F. D.; Vukanovic, V.; Taylor, G. N. *Plasma Deposition, Treatment, and Etching of Polymers*; Academic Press, Inc.: San Diego, CA, 1990. (b) Boenig, H. V. *Fundamentals of plasma chemistry and technology*; Technomic Pub. Co.: Lancaster, PA, 1988.(c) Joubert, O.; Paniez, P.; Pelletier, J.; Pons, M. *Appl. Phys. Lett.* **1991**, *58*, 959–961.
(27) (a) Herbert, S.; Shinozaki, D. M.; Collacott, R. J. *J. Mater. Sci.* **1996**, *31*, 4655–4661. (b) Riekerink, M. B. O.; Terlingen, J. G. A.; Engbers, G. H. M.; Feijen, J. *Langmuir* **1999**, *15*, 4847–4856.
(28) Daubeny, R. d. P.; Bunn, C. W. *Proc. R. Soc. London, A Math. Phys. Sci.* **1954**, *226*, 531–542.
(29) Fischer, E. W.; Fakirov, S. *J. Mater. Sci.* **1976**, *11*, 1041–1065.
(30) Hyun, J.; Aspnes, D. E.; Cuomo, J. J. *Macromolecules* **2001**, *34*, 2395–2397.
(31) Kirov, K. R.; Assender, H. E. *Macromolecules* **2005**, *38*, 9258–9265.
(32) Cole, K. C.; Ajji, A.; Pellerin, E. *Macromolecules* **2002**, *35*, 770–784.
(33) Kawakami, D.; Burger, C.; Ran, S. F.; Avila-Orta, C.; Sics, I.; Chu, B.; Chiao, S. M.; Hsiao, B. S.; Kikutani, T. *Macromolecules* **2008**, *41*, 2859–2867.
(34) Cross, J. H.; Lemay, M. W.; McClure, D. J. *J. Vac. Sci. Technol. A* **1985**, *3*, 495–498.
(35) Matthews, S. R.; Hwang, Y. J.; McCord, M. G.; Bourham, M. A. *J. Appl. Polym. Sci.* **2004**, *94*, 2383–2389.
(36) Tsougeni, K.; Vourdas, N.; Tserepi, A.; Gogolides, E.; Cardinaud, C. *Langmuir* **2009**, *25*, 11748–11759.
(37) (a) Northen, M. T.; Turner, K. L. *Sensor. Actuat. A-Phys.* **2006**, *130*, 583–587. (b) Northen, M. T.; Turner, K. L. *Curr. Appl. Phys.* **2006**, *6*, 379–383.
(38) Bruce, R. L.; Weilnboeck, F.; Lin, T.; Phaneuf, R. J.; Oehrlein, G. S.; Long, B. K.; Wilson, C. G.; Vegh, J. J.; Nest, D.; Graves, D. B. *J. Appl. Phys.* **2010**, *107*, 084310–5.

(39) (a) Di Mundo, R.; De Benedictis, V.; Palumbo, F.; d'Agostino, R. *Appl. Surf. Sci.* **2009**, *255*, 5461–5465. (b) Kaless, A.; Schulz, U.; Kaiser, N. *Self-organized antireflective nanostructures on PMMA by ion etching* **2005**, 59651N.
(40) Adams, G. C. *Polym. Eng. Sci.* **1976**, *16*, 222–226.
(41) (a) Beake, B. D.; Leggett, G. J.; Shipway, P. H. *Polymer* **2001**, *42*, 7025. (b) Beake, B. D.; Shipway, P. H.; Leggett, G. J. *Wear* **2004**, *256*, 118–125.
(42) (a) Zhang, Z. Y.; Boyd, I. W.; Esrom, H. *Surf. Interface Ana.* **1996**, *24*, 718–722. (b) Lazare, S.; Srinivasan, R. *J. Phys. Chem.* **1986**, *90*, 2124–2131. (c) Brezini, A. *Phys. Status Solidi A-Appl. Res.* **1993**, *135*, 589–596. (d) Novis, Y.; Pireaux, J. J.; Brezini, A.; Petit, E.; Caudano, R.; Lutgen, P.; Feyder, G.; Lazare, S. *J. Appl. Phys.* **1988**, *64*, 365–370.
(43) Bityurin, N.; Arenholz, E.; Arnold, N.; Bauerle, D. *Phys. Rev. E* **2007**, *75*, 41603.
(44) Arenholz, E.; Heitz, J.; Wagner, M.; Bauerle, D.; Hibst, H.; Hagemeyer, A. *Appl. Surf. Sci.* **1993**, *69*, 16–19.
(45) Bäuerle, D. In *Laser Processing and Chemistry*; 3rd ed.; Springer: Berlin and Heidelberg, Germany, 2000.
(46) Greiner, C.; Buhl, S.; del Campo, A.; Arzt, E. *J. Adhes.* **2009**, *85*, 646–661.
(47) (a) Yoon, E. S.; Singh, R. A.; Kong, H.; Kim, B.; Kim, D. H.; Jeong, H. E.; Suh, K. Y. *Tribol. Lett.* **2006**, *21*, 31–37. (b) Majidi, C.; Groff, R. E.; Maeno, Y.; Schubert, B.; Baek, S.; Bush, B.; Maboudian, R.; Gravish, N.; Wilkinson, M.; Autumn, K.; Fearing, R. S. *Phys. Rev. Lett.* **2006**, *97*, 76103. (c) Aksak, B.; Sitti, M.; Cassell, A.; Li, J.; Meyyappan, M.; Callen, P. *Appl. Phys. Lett.* **2007**, *91*, 61906.